CO2 photoreduction to methanol over Nb and N co-doped TiO2 aerogel deposited CuxO

Miaomiao Wen, Mourad Benabdesselam, Christian Beauger

Journal of CO2 Utilization 81 (2024) 102719

Contents lists available at ScienceDirect

Journal of CO2 Utilization

journal homepage: www.elsevier.com/locate/jcou

CO_2 photoreduction to methanol over Nb and N co-doped TiO_2 aerogel deposited Cu_xO

Miaomiao Wen [a], Mourad Benabdesselam [b], Christian Beauger [a,*]

[a] Mines Paris, PSL University, Centre for Processes, Renewable Energy and Energy Systems (PERSEE), Sophia Antipolis, 06904, France
[b] Université Côte d'Azur, CNRS, Institut de Physique de Nice – INPHYNI UMR 7010, F-06200, Nice, France

ARTICLE INFO

Keywords:
Nb and N co-doped TiO_2
CO_2 photoreduction
Methanol
Cu_xO
Aerogel

ABSTRACT

Global warming is primarily caused by greenhouse gases such as CO_2. One smart solution to mitigate its impact is to convert CO_2 into hydrocarbons through photoreduction processes. In this work, CO_2 was photo-catalytically reduced over new aerogel-based materials to produce methanol, using a solar simulator and a specifically designed photoreactor.

Cu-loaded Nb and N co-doped TiO_2 aerogels (Cu/ATiO$_2$: Nb, N) were synthesized by the sol-gel method followed by supercritical CO_2 drying and annealing in a controlled atmosphere. The obtained photocatalysts benefit from the peculiar properties of aerogels with high specific surface area (88 m^2/g) and porosity. N and Nb doping improved the electronic and optical properties, resulting in a significantly improved visible light absorption compared to pure TiO_2 aerogel (ATiO$_2$) or commercial catalyst P25. Cu_xO nanoparticles, smaller than 5 nm and uniformly distributed on the surface of aerogels, contribute to the improvement of the conversion efficiency. Used for CO_2 photoreduction, one of the best-reported methanol yields (1.69 ± 0.05 mmol/g_{cat}/h) was obtained, and the impact of Cu, Nb, and N on methanol production was studied.

1. Introduction

Carbon dioxide (CO_2) is a major greenhouse gas that contributes to global warming and climate change [1]. Therefore, it is imperative to find a green, economical, and efficient solution for its conversion and utilization. However, CO_2 is the most thermodynamically stable compound of carbon with a standard enthalpy of formation of –393.5 kJ/mol and a C═O Bond energy E = 803 kJ/mol (298.15 K). Hence, the activation of CO_2 requires a lot of energy [2,3]. Traditional methods (e.g., thermal catalysis) are not efficient. On the contrary, artificial photosynthesis enables CO_2 reduction under mild conditions [4,5]. Therefore, developing efficient and stable photocatalysts that convert CO_2 into useful fuels such as formic acid, methane, formaldehyde, methanol, ethanol, etc. is crucial for the development of CO_2 photoreduction processes.

Among different semiconductors, titanium dioxide (TiO_2), with a band gap of 3.2 eV in its anatase form, has attracted considerable attention due to its abundance, low cost, high stability, and wide applicability [6]. Inoue et al. observed in 1979 that CO_2 can be catalytically converted to methanol and formic acid using TiO_2 as a photocatalyst [7], paving the way to its utilization in this area. However, raw TiO_2 has low visible light absorption, due to its wide bandgap, which leads to fast recombination of photogenerated charge carriers and shows low CO_2 adsorption capacity [8,9]. To overcome these drawbacks, many strategies have been proposed to modify TiO_2, such as doping [10], heterojunction formation [11], surface modification [12], and hybridization with other materials [13].

The doping of TiO_2 with various elements can increase its photocatalytic activity from the creation of new energy levels in the bandgap. Such energy levels can be located either near the conduction or the valence band [14] depending on the type of dopant, like metal [15,16] and non-metal [17,18]. For example, doping TiO_2 with silver (Ag) can enlarge its visible light absorption range, lowering the bandgap to 2.5 eV [19]. Moreover, the creation of Ti–Ag–O also promotes more efficient charge transfer and separation after irradiation [19]. Similarly, Lantanum (La) doping was reported to impact the structural, optical, and photoluminescence properties of TiO_2 nanocrystals [20]. Lattice-doped TiO_2 nanofibers with enhanced photocatalytic properties effectively convert N_2 to NH_3 (14783 μmol/L/g_{cat}) under visible light [21].

Niobium (Nb^{5+}) (0.64 Å) has a similar ionic radius to Ti^{4+} (0.605 Å), allowing doping by substitution [22,23]. Such doping will generate Nb°_{Ti}

* Correspondence to: Mines Paris, Université PSL, Centre Procédés Energies Renouvelables et Systèmes Energétiques (PERSEE), Sophia Antipolis, 06904, France.
E-mail address: christian.beauger@minesparis.psl.eu (C. Beauger).

https://doi.org/10.1016/j.jcou.2024.102719
Received 5 December 2023; Received in revised form 9 February 2024; Accepted 21 February 2024
Available online 7 March 2024

defects compensated with additional free electrons in TiO_2. These free electrons can be trapped by Ti^{4+} or oxygen vacancies ($V_O^{\circ\circ}$) to generate respectively Ti^{3+} or V_O°. Because Nb^{5+} is an electron donor, the introduction of Nb can increase the electrical conductivity of the samples [24,25] Nb^{5+} doping might also introduce interstitial O defects, [26] with energy states lying upon the VB of TiO_2, giving rise to yellow samples [27]. With increasing Nb concentration, the optical band gap becomes increasingly narrow (2.93 eV→2.75 eV for 10 mol% Nb) [28]. Nb-doped TiO_2 microspheres have been reported to exhibit higher photocatalytic rates than undoped TiO_2 for the degradation of gaseous acetaldehyde [28].

However, the concentration of the dopant in the host matrix has to be precisely controlled. Indeed, too high a concentration can result in a quenching of the expected property and introduce excessive structural defects which can affect the stability of the crystal.

For non-metal doping, C-doping can introduce oxygen vacancies and defects in TiO_2, which can also increase visible light absorption and surface reactivity [29]. N-doping can create new energy levels or modify the band structure of TiO_2, which can facilitate the transfer and separation of charge carriers and reduce their recombination rate [30–33]. Co-doping with metal and non-metal elements is also an option for modifying TiO_2. N, Eu co-doped TiO_2 enhanced photocatalytic reduction of CO_2 into CH_4 (13.48 $\mu mol \cdot g_{cat}^{-1} \cdot h^{-1}$), which was reported to be about 12 times higher than that of pure TiO_2, thanks to the synergistic effect of Eu and N. The modification did not only effectively increase the surface area of N-Eu/TiO_2 and inhibit crystallization of TiO_2, but also reduced the band gap of TiO_2 [34].

As another example, Ce/N co-doping highly affects the structure and activity of TiO_2. As the Ce concentration in the catalyst was increased the crystallinity and crystal size of the co-doped samples decreased with an increase in BET specific surface area [35]. Depositing metal (e.g. Fe, [36] Cu, [37] Ag, [38] Au, [39] and Pt [40]) on the surface of TiO_2 is also an appropriate method for improving the separation of electron-hole pairs through the established metal-semiconductor Schottky junction. This not only helps extract the photogenerated electrons but also dramatically reduces the energy barrier for proton reduction.

In the realm of photocatalytic materials, the surface area plays a pivotal role, with a higher surface area correlating to increased catalytic activity [41–44]. In photocatalytic CO_2 reduction, TiO_2 aerogels are distinguished by their high specific surface areas (S_{BET}), which markedly enhance their photocatalytic performance [45]. 3D structured TiO_2--based aerogel photocatalyst showed a high efficiency for the degradation of toluene gas. The toluene-removal rate of Pt–TiO_2/RGO aerogel was 60% higher than that of the pure RGO aerogel, and 56% higher than that of the bare TiO_2 nanofibers [46]. Pd-TiO_2 aerogels are approximately 3.5-fold more active for H_2 evolution than Pd-TiO_2 powders, giving evidence that the porous structure favors light-harvesting and reagent transport, making them superior photocatalysts [47].

Aerogels are known to exhibit large specific surface area and pore volume, which can be highly beneficial for CO_2 adsorption and activation, enlarging the contact surface between the reactants and the catalyst. [48,49] In this paper, we report the synthesis and characterization of a new photocatalyst, developed based on the previous work of our group [50].

Nb, N-codoped TiO_2 aerogels were prepared to support Cu oxides (Cu_xO) nanoparticles deposited through an in-situ synthesis route. TiO_2 aerogels are recognized as highly porous materials, which can enhance light absorption and charge separation [45].

Here, we have studied the combined role of doping TiO_2 aerogels with niobium and nitrogen with that of Cu_xO nanoparticles deposited on their surface. The photocatalytic activity of as-prepared photocatalysts was investigated for photocatalytic reduction of CO_2. Notably, this methodology resulted in one of the best-reported methanol yields, achieving an impressive rate of 1.69 ± 0.05 mmol/g_{cat}/h. The relation between the structure, morphology, optical properties, and photocatalytic activity was discussed in detail.

Table 1
List of samples synthesized and studied in this work.

Name	Calcination (550 °C)
$ATiO_2$	Air
$ATiO_2$: **Nb**	Air
$ATiO_2$: **N**	NH_3
$ATiO_2$: **Nb, N**	NH_3
Cu/$ATiO_2$	Air
Cu/$ATiO_2$: **Nb**	Air
Cu/$ATiO_2$: **N**	NH_3
Cu/$ATiO_2$: **Nb, N**	NH_3

2. Experimental section

2.1. Chemicals

All chemicals were of analytical grade and used without further purification. Copper nitrate ($Cu(NO_3)_2$•3 H_2O, Alfa Aesar), Nitric acid (HNO_3, 2 M, Alfa Aesar), Tetrabutyl titanate ($Ti(OBu)_4$, $C_{16}H_{36}O_4Ti$, Alfa Aesar), Niobium isopropoxide ($Nb(OiPr)_5$, $C_{15}H_{35}NbO_5$, 10% w/v in isopropanol/hexane (50:50) (10 at%), Alfa Aesar), Absolute ethanol (CH_3CH_2OH, Alfa Aesar), Isopropanol (iPrOH, C_3H_8O, Alfa Aesar), Deionized water (D.I., Homemade), Argon (Ar, 99.9999%), Ammonia (NH_3, 10 w.t. % in N_2).

2.2. Preparation of catalysts

Aerogels were synthesized starting from a classical sol-gel route based on alkoxides, [51] and already experienced in a previous study [52]. The following parameters have been selected for the whole study: R = $H_2O/Ti(OBu)_4$ = 3.4 (mol/mol), C = $HNO_3/Ti(OBu)_4$ = 0.07 (mol/mol), and S = iPrOH/$Ti(OBu)_4$ = 15 (mol/mol).

Briefly, 10.96 ml of $Ti(OBu)_4$, 10.01 ml of $Nb(OiPr)_5$, and 0.382 g Cu $(NO_3)_2$•3 H_2O (5 wt%) in 15 ml iPrOH were mixed with thorough stirring and noted as solution A. Similarly, 0.84 ml D.I. water, 1.12 ml HNO_3, and 16 ml iPrOH were mixed with thorough stirring to obtain a solution marked as B.

Solution B was added dropwise into solution A within 30 s, with vigorous stirring for 1 min, then left to stand for gelation. The resulting gel was aged at room temperature for 72 hours, and then washed with isopropanol 3 times a day for 3 days to remove H_2O and unreacted chemicals. Finally, supercritical CO_2 drying (SC CO_2) was carried out to obtain Nb-doped TiO_2 aerogel. Cu-contained aerogel samples were prepared with the addition of $Cu(NO_3)_2$ in solution A.

For N-doping, aerogels were calcined under NH_3 atmosphere for 45 mins at 550 °C (ramp-up and cool-down under N_2 at 5 °C /min). The obtained powder was labeled Cu/$ATiO_2$: Nb, N (A standing for aerogel). This post-treatment was named as NH_3 treatment. Cu/$ATiO_2$: N and $ATiO_2$: Nb, N were also obtained by applying this NH_3 treatment to corresponding aerogels. Other samples were calcined in Air (550 °C, 2 h) and labeled $ATiO_2$, $ATiO_2$: Nb, Cu/$ATiO_2$, and Cu/$ATiO_2$: Nb.

The list of samples is presented in Table 1.

2.3. Characterization

X-ray diffraction (XRD) patterns were collected using a powder diffractometer (MPD PANalytical X'Pert Pro) operated at 45 kV, with CuKa radiation (λ = 0.154 nm). Data were collected in steps of 0.05° from 10 ° to 90 ° in 2θ mode with Pixcel counter.

The X-ray photoelectron spectroscopy (XPS) analyses were carried out using a Thermo Scientific K-Alpha system. XPS analysis was repeated 5 times on the same sample. The positions of all binding energies were calibrated using the C1*s* line at 284.8 eV.

Scanning electron microscopy (SEM) observations were recorded

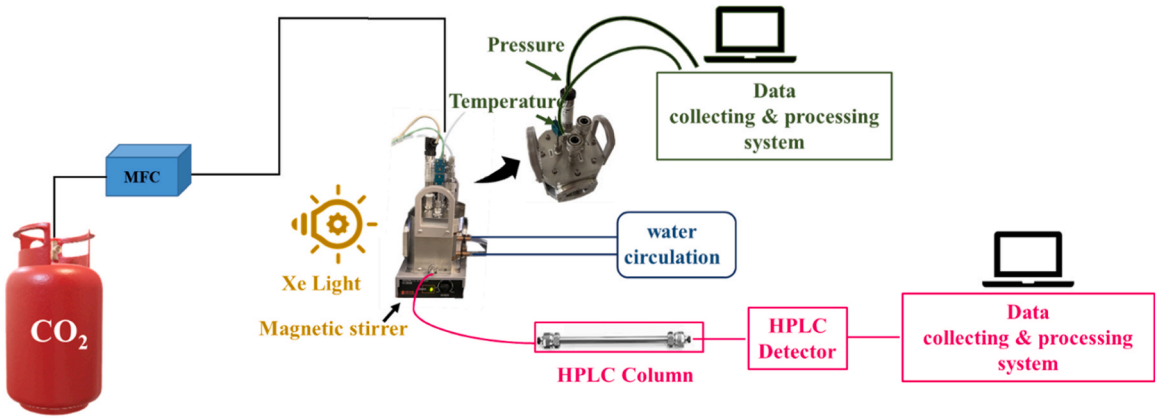

Scheme 1. Sketch schematic of test bench.

with a MAIA3 with a 3 kV electron beam. The composition has been analyzed by energy dispersive X-ray spectroscopy (EDX) at 15 kV, performed with a Philips XL30.

Transmission electron microscopy (TEM, Thermo Fisher Spectra 200, operated at 200 kV and equipped with a cold filed emission gun and a Cs aberration probe corrector) analyses in high resolution TEM (HRTEM) mode and in scanning TEM (STEM) mode.

Solid-state UV–visible diffuse reflectance spectra (UV-Vis DRS) were recorded at room temperature using the Cary 500 UV–VIS–NIR spectrophotometer. Polytetrafluoroethylene standard was used as the reference. The bandgap was determined according to Kubelka-Munk treatment. Two values for each sample were averaged. They were obtained by intersecting extreme tangents to the curve in the most vertical area with the horizontal coordinate.

Isothermal N_2 sorption experiments were performed with BELSORP MINI X. The BET model was applied to calculate the specific surface area of samples (S_{BET}). Each sample was tested twice to obtain an average value of S_{BET}.

2.4. Evaluation of catalytic performance

The catalytic reaction was carried out in a specifically designed micro-autoclave equipped with sapphire windows and placed in a black box. Sketch schematic of test bench was present in Scheme 1. A 100 W Xe-light source (Oriel® LCS-100^{TM} Small Area Sol1A, Newport) was used as a solar simulator, the photocatalytic experiments were conducted under a broad range of wavelengths, encompassing the entire spectrum of light that the Xe lamp emits, thereby utilizing the complete range of photon energies available from UV to visible light. The photocatalyst (200 mg), and Na_2CO_3 (400 mg) were added in H_2O (100 ml) and sonicated for 30 min. The suspension was transferred into the reactor and purged with CO_2 (1 L/h) gas for 30 min in the dark. The lamp was then switched on to illuminate the sample and the temperature and the pressure were recorded during the experiment. Liquid aliquots were sampled at regular intervals using a sampling port at the bottom of the reactor and analyzed with high-performance liquid chromatography (HPLC, Shimadzu LC 20). The HPLC is equipped with a typical sugar column (HPLC Column SUGAR SH1821, 6 μm, 8 ×300 mm, Shodex) using 5 mM H_2SO_4 as mobile phase, a UV detector, and a refractive indexing detector (RID). The gas was analyzed using an Agilent 3000 A MICRO GC, which is equipped with a Thermal Conductivity Detector (TCD). The analysis revealed that methanol was the sole product identified in the reaction liquid, with no detectable products in the gas phase.

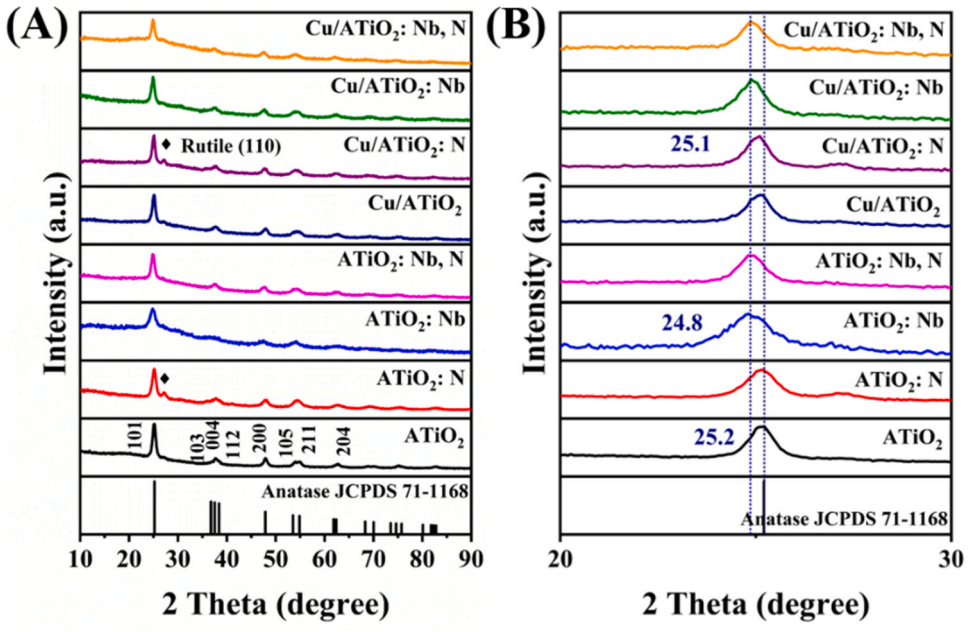

Fig. 1. (A) XRD patterns of synthesized samples and (B) enlarge image of 20−30° zone.

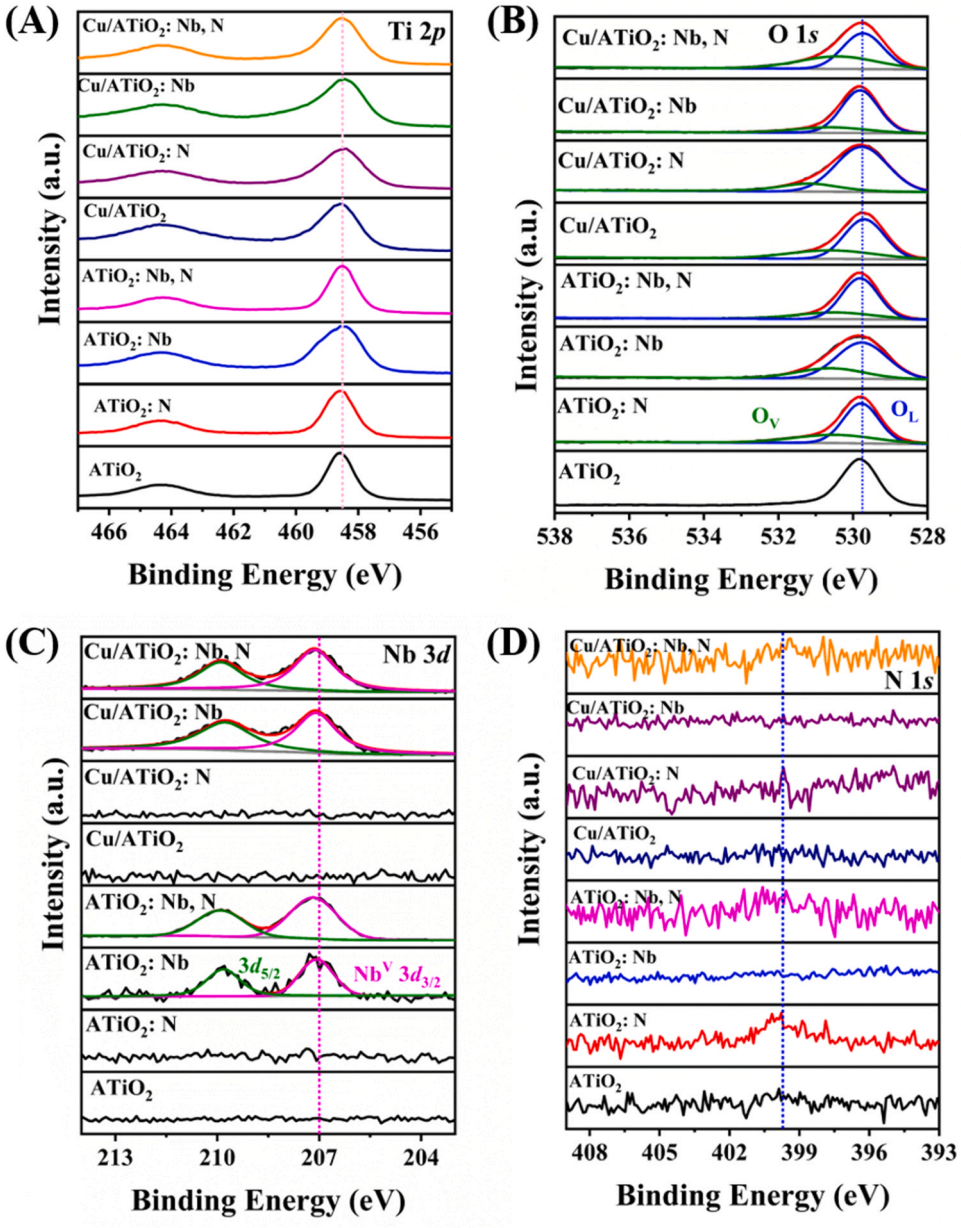

Fig. 2. XPS spectra of synthesized samples: (A) Ti 2*p*, (B) O 1 *s* O_L = lattice oxygen, O_V = oxygen vacancies, (C) Nb 3*d,* and (D) N 1 *s*.

3. Results and discussion

Before evaluating their photocatalytic ability for CO_2 reduction, aerogel samples were deeply characterized.

3.1. Physicochemical characterization

All samples have been characterized with XRD, XPS, N_2 sorption, SEM, and TEM to analyze their morphology, composition, and structure which are important features considering the foreseen application.

Fig. 1 shows the X-ray diffraction spectra (XRD) of the different samples and P25 (Figure S3), TiO_2 aerogels doped with Nb and N ($ATiO_2$: Nb, N), and their counterparts loaded with Cu ($Cu/ATiO_2$: Nb, N). All patterns show the crystalline phase of Anatase TiO_2 (JCPDS 71–1168). No other oxide phase could be detected showing that Nb is most probably included in the crystalline structure of TiO_2. This is confirmed by the slight blue shift of the (101) peak at 25.2° (Fig. 1B), a shift only observed for the Nb-doped samples, as in our previous work [50]. This can be ascribed to a cell distortion resulting from doping because the ionic radius of Nb^{5+} (0.64 Å) is slightly larger than that of Ti^{4+} (0.605 Å).

The (110) peak of Rutile was clearly observed for the samples doped only with N, $ATiO_2$: N, and $Cu/ATiO_2$: N. It appears much weaker on other samples. The NH_3 treatment may lower the TiO_2 phase transfer temperature which should rise above 600 °C. We have already experienced such an effect of a reducing calcination atmosphere in our previous work [50]. This peak appears with a much lower intensity on XRD patterns of other samples, even those co-doped with N, $ATiO_2$: Nb, N and $Cu/ATiO_2$: Nb, N. For the latter, this may result from the presence of Nb, which in turn is increasing the TiO_2 phase transfer temperature as also reported in our previous study, thus probably here counterbalancing the effect of NH_3 treatment [50].

In all Cu-loaded samples, the peaks of Cu_xO were not observed, maybe due to the small size of the Cu_xO particles, uniformly distributed in the sample.

As shown in Table S1, the crystallite size calculated from the (101)

Table 2
Ti 2p, O 1 s, and Nb 3d peaks position as determined for the different samples analyzed.

samples	Ti 2*p* (eV)		O 1 *s* (eV)		Nb 3*d* (eV)	
	Ti $2p_{1/2}$	Ti $2p_{3/2}$	O_V	O_L	Nb $3d_{5/2}$	Nb $3d_{3/2}$
Cu/ATiO$_2$: Nb, N	464.28	458.51	530.67	529.78	209.89	207.17
Cu/ATiO$_2$: Nb	464.31	458.42	530.87	529.86	209.80	207.13
Cu/ATiO$_2$: N	464.28	458.47	531.16	529.77	-	-
Cu/ATiO$_2$	464.30	458.53	530.88	529.78	-	-
ATiO$_2$: Nb, N	464.25	458.53	530.85	529.83	209.93	207.17
ATiO$_2$: Nb	464.25	458.51	530.83	529.80	209.94	207.13
ATiO$_2$: N	464.30	458.52	531.12	529.74	-	-
ATiO$_2$	464.25	458.53	-	529.81	-	-

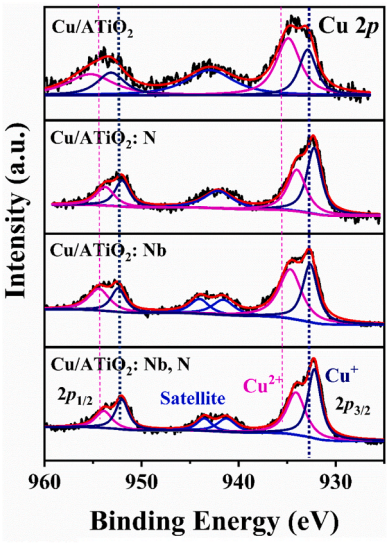

Fig. 3. Cu 2*p* XPS spectra of Cu loaded ATiO$_2$, ATiO$_2$: N, ATiO$_2$: Nb and ATiO$_2$: Nb, N.

peak is very similar for all samples, close to 12 nm. There is no significant effect either of the doping or the metal loading.

The Ti 2*p* X-ray photoelectron spectra (XPS) of all samples show peaks at ~464.3 eV and ~458.5 eV attributed to Ti^{4+} Ti $2p_{1/2}$ and Ti $2p_{3/2}$ respectively (Fig. 2A) [53]. As presented in Table 2, their positions are very similar whatever the samples. The doping or the presence of Cu seems to not affect the binding energy of Ti in the analyzed samples.

The XPS O 1 *s* peak can be separated into two peaks at ~529.8 eV and ~530.8 eV corresponding to lattice oxygen (O_L) and oxygen vacancies (O_V) respectively (Fig. 2B) [54]. The latter (O_V) appears only for doped samples, as a result of charge balancing, thus evidencing the successful doping of the samples. As for Ti 2*p*, no significant shift in the position of the O species peaks was observed for the different samples, (Table 2), except for samples doped only with N, ATiO$_2$: N, and Cu/ATiO$_2$: N.

Nb could be detected in our samples (Fig. 2C). The peaks at ~209.9 eV and ~207.2 eV are attributed to Nb^{5+} Nb $3d_{5/2}$ and Nb $3d_{3/2}$ respectively [55]. Here also, still no significant shift in the peak positions as presented in Table 2.

After N-doping, a peak corresponding to N 1 *s* was expected at ~400 eV [56]. If this peak can clearly be observed in Fig. 2D for ATiO$_2$: N, it can hardly be detected for other N-doped samples, maybe due to only a very small amount of N introduced in the TiO$_2$ lattice.

The XPS spectra of Ti 2*p*, O *1 s*, and Nb 3*d* are not different between ATiO$_2$, ATiO$_2$: Nb, ATiO$_2$: Nb, N, Cu/ATiO$_2$, Cu/ATiO$_2$: N, Cu/ATiO$_2$: Nb, and Cu/ATiO$_2$: Nb, N, indicating that the surface electronic

Table 3
Cu 2p Analyses of Cu loaded ATiO$_2$, ATiO$_2$: N, ATiO$_2$: Nb and ATiO$_2$: Nb, N.

Samples	Cu 2*p*				
	Cu $2p_{1/2}$		Cu $2p_{3/2}$		Cu^+/Cu^{2+} Peak surface area ratio
	Cu^{2+}	Cu^+	Cu^{2+}	Cu^+	
Cu/ATiO$_2$	954.89	953.10	934.90	932.87	0.80
Cu/ATiO$_2$: N	953.90	951.98	934.05	932.30	1.21
Cu/ATiO$_2$: Nb	954.39	952.37	934.69	932.70	0.77
Cu/ATiO$_2$: Nb, N	954.02	952.04	934.10	932.20	1.21
Cu/ATiO$_2$: Nb-2 (calcination under N_2)	954.33	952.17	934.35	932.34	0.97

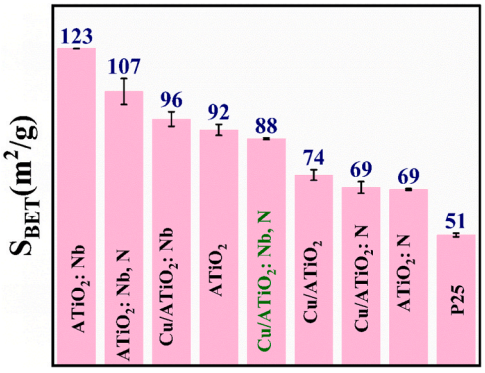

Fig. 4. Specific surface area (S_{BET}) of synthesized samples and commercial catalyst P25* *Instrumental error [%] = 0.6.

structure of as-prepared catalysts before and after doping and loading remain stable, which is an important property of photocatalysts.

Fig. 3 shows the Cu 2*p* XPS spectra obtained for the samples loaded with Cu: Cu/ATiO$_2$, Cu/ATiO$_2$: N, Cu/ATiO$_2$: Nb, and Cu/ATiO$_2$: Nb, N. The peaks for Cu $2p_{1/2}$ and Cu $2p_{3/2}$ were separated to bring out peaks corresponding to Cu^{2+} and Cu^+. Detailed information on the peak position is presented in Table 3 and Table S2.

Taking Cu $2p_{3/2}$ as an example, the peak at ~934.10 eV is attributed to Cu^{2+} and the peak at ~932.20 eV is attributed to Cu^+ [57]. The peak position of Cu^{2+} and Cu^+ both shifted to a lower binding energy (redshift) after N doping: see the comparison between Cu/ATiO$_2$: N and Cu/ATiO$_2$ (−0.99/−0.85 eV for Cu^{2+} $2p_{1/2}/2p_{3/2}$, −1.12/−0.57 eV for Cu^+ $2p_{1/2}/2p_{3/2}$) and between Cu/ATiO$_2$: Nb, N and Cu/ATiO$_2$: Nb (−0.37/−0.59 eV for Cu^{2+} $2p_{1/2}/2p_{3/2}$, −0.33/−0.50 eV for Cu^+ $2p_{1/2}/2p_{3/2}$). This red shift represents an increase of the electron density around Cu, resulting from a modification of their local chemical environment after NH_3 treatment [58]. Considering the difference in electronegativity between N (3.04) and O (3.44) it is supposed to replace in TiO$_2$ structure, [59] we may see here another evidence of N-doping. Moreover, this would indicate a close connection of Cu with N or O in the structure.

It is also clear from Fig. 3 that an inversion of the Cu^{2+} and Cu^+ peak relative intensity arose after NH_3 treatment compared to samples calcined under air. Note that an intermediate value was obtained after calcination under N_2 (0.97), see Table 3 and Figure S1. The comparison revealed a higher Cu^+ content for the samples calcined under NH_3, showing a reduction of Cu^{2+} during the treatment, in agreement with the modification of the electron density around Cu described before.

The specific surface area (S_{BET}) of our samples was analyzed concerning their composition and compared to that of P25 (Fig. 4). The N_2 sorption isotherms of Cu/ATiO$_2$: Nb, N curve was shown in Figure S4. The higher the S_{BET} the better for photocatalytic performance.

Confirming the expected properties of aerogels, [45] our obtained TiO$_2$ aerogel (ATiO$_2$) showed a higher S_{BET} (92 m^2/g) than the

Table 4
Comparative Analysis of TiO_2-Based Photocatalysts: Synthesis Methods, Applications, and Specific Surface Areas.

Sample	synthesis method	calcination temperature (°C)	applications	S_{BET} (m^2g^{-1})	Ref
$ATiO_2$	Sol-Gel	550	CO_2 photoreduction	91	this work
$ATiO_2$: Nb (10 at%)	Sol-Gel	550	CO_2 photoreduction	123	this work
Cu/$ATiO_2$: Nb, N	Sol-Gel	550	CO_2 photoreduction	88	this work
P25	-	-	commercial catalysts	50	-
TiO_2	Sol-Gel	500	photodegradation	67.66	[60]
TiO_2 Microspheres	Reverse microemulsion	500	photodegradation	23.6	[28]
Nb 10 mol% doped TiO_2 Microspheres	Reverse microemulsion	500	photodegradation	79.6	[28]
polymorphs TiO_2	Sol-Gel	400	photodegradation	Anatase 9.33 Rutile 5.13	[61]
TiO_2 Aerogel	Sol-Gel	500	photodegradation	136	[62]
TiO_2 Aerogel	Sol-Gel	400	photodegradation	135	[45]
TiO_2 Aerogel	Sol-Gel	550	photodegradation	82	[51]

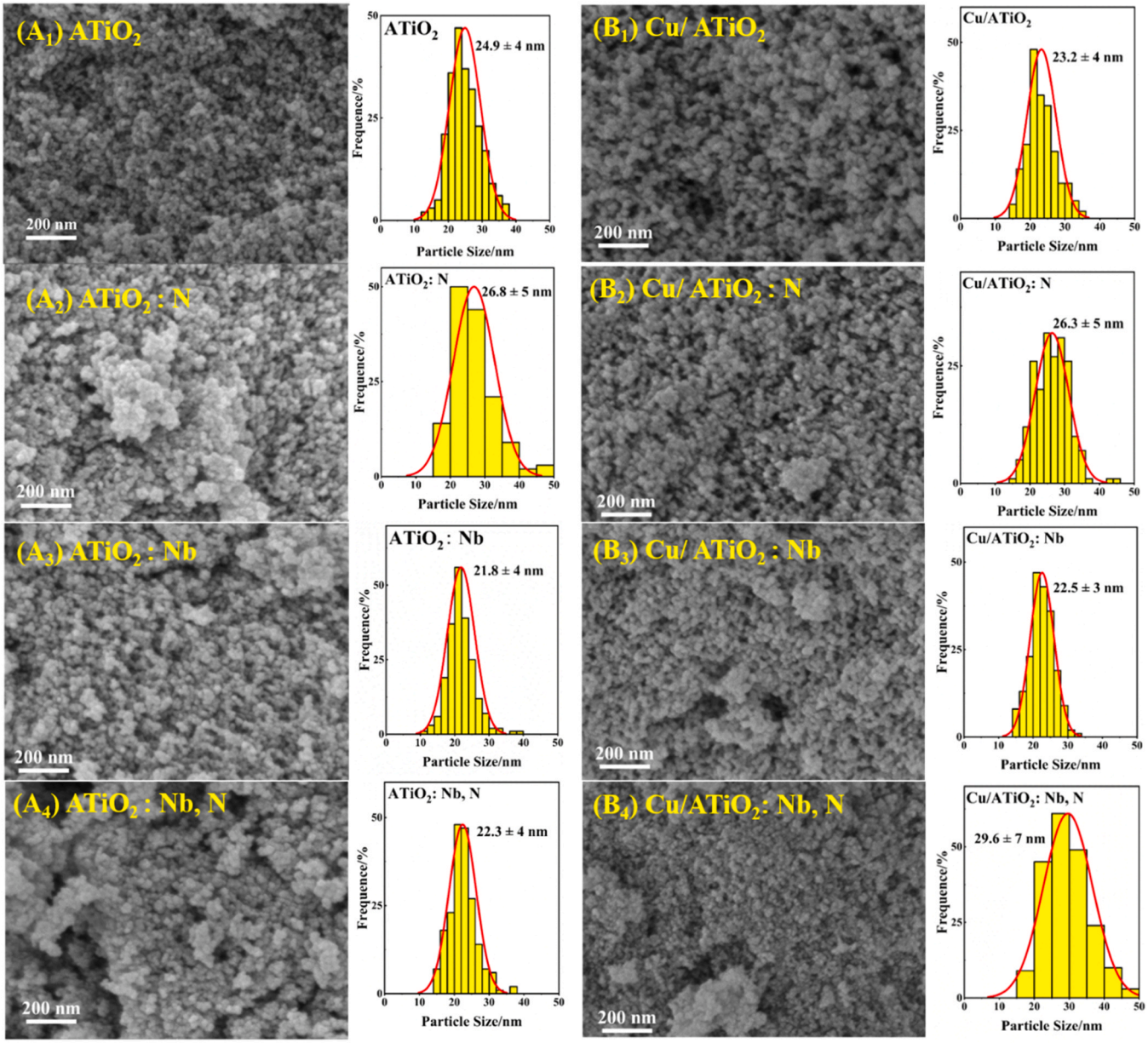

Fig. 5. SEM images and Particle size distribution of synthesized samples (A_i) $ATiO_2$, $ATiO_2$: N, $ATiO_2$: Nb, and $ATiO_2$: Nb, N, (B_i) Cu loaded counterparts. *Particle size distribution was statistics based on counting 200 particles.

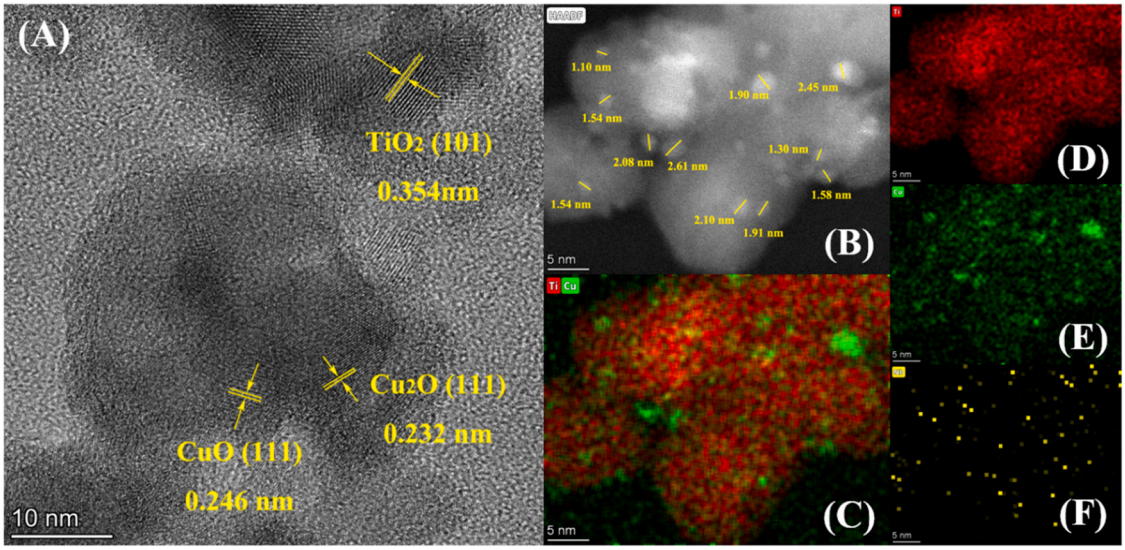

Fig. 6. (A) HAADF-STEM image of Cu/ATiO$_2$: Nb, N, (B) Measured Cu$_x$O particle size and (C) EDS elemental mapping of Ti (D), Cu (E), and Nb (F).

commercial catalyst P25 (51 m^2/g). The S_{BET} was significantly increased after doping with Nb (123 m^2/g for ATiO$_2$:Nb), in agreement with our previous study [50]. Present in Table 4, is the S_{BET} value in the literature, TiO$_2$ aerogels have an obviously high surface specific area.

The Cu-loaded samples maintained a high specific surface area, 74 and 96 m^2/g respectively for Cu/ATiO$_2$ and Cu/ATiO$_2$: Nb, despite a notable decrease of about 20%.

The NH$_3$ post-treatment, applied to dope samples with N resulted in a slight decrease of the specific surface area, −5 m^2/g for Cu/ATiO$_2$: N (69 m^2/g), −16 m^2/g for ATiO$_2$: Nb, N (107 m^2/g) and −8 m^2/g for Cu/ATiO$_2$: Nb, N (88 m^2/g), which is quite reasonable.

Such a systematic decrease can be accounted for the temperature of the NH$_3$ treatment which is responsible for a slight particle size increase as evidenced by the SEM pictures (Fig. 5).

Fig. 5 presents the SEM images for ATiO$_2$ and its various doped forms, including ATiO$_2$: N, ATiO$_2$: Nb, and ATiO$_2$: Nb, N, as well as their Cu-loaded variations. Consistent with our previous studies [50], the TiO$_2$ aerogels display a texture that appears relatively dense due to the agglomeration of roughly spherical particles and looks slightly dense. The apparent density is however difficult to measure since the monolithic nature was lost during supercritical drying and calcination.

The particle size of our aerogels stands between 22 nm and 30 nm with quite uniform distribution. The doping with Nb leads to a decrease in the particle size of TiO$_2$ aerogels from 25 to 22 nm in diameter (modulo the accuracy of the method), which is consistent with the conclusion of N$_2$ sorption analysis (Fig. 4). Except for Cu/ATiO$_2$: Nb, N, the presence of Cu did not impact the mean particle size of the samples. The small size of the particles, on top of resulting in a large specific surface area, is beneficial to the refraction of the incident light on the catalyst surface, thus improving the photocatalytic efficiency [63].

The presence of Cu in the samples was confirmed by TEM observations which also gave some information on the size of the Cu$_x$O particles (Fig. 6).

Fig. 6A shows the HAADF-STEM image of Cu/ATiO$_2$: Nb, N. Two families of lattice spaces could be analyzed. The lattice space of 0.354 nm corresponds to Anatase TiO$_2$ (101) [64]. The lattice spaces of 0.246 nm and 0.232 nm can be attributed to CuO (111) and Cu$_2$O (111), respectively [65], in agreement with the results obtained by XPS (Cu 2*p*, Fig. 3). Comparison between Fig. 6B, C, and E, led to the conclusion that the small particles observed in Fig. 6B most probably correspond to Cu$_x$O. Their diameter roughly stands between 1.5 and 3 nm, which confirms the difficulty of detecting any Cu$_x$O species with XRD (Fig. 1).

Nb could be detected (Fig. 6F), apparently uniformly distributed over the image. The amount is however too small to discuss further.

The presence of Cu$_x$O species as homogeneously dispersed nanoparticles may facilitate the CO$_2$ reduction reaction and contribute to the fast migration of intermediate species for better efficiency.

3.2. Optical characterization

UV–vis diffuse reflectance spectroscopy (UV-Vis DRS) was used to characterize the domain of light absorption of our materials and to determine their bandgap (Fig. 7).

A strong adsorption band (< 400 nm) is found for all samples (Fig. 7 A), which is caused by the intrinsic interband absorption of TiO$_2$ [66].

Our TiO$_2$ aerogel absorbs a little bit more light than P25 and even a little bit more after Nb doping. The difference in absorption between ATiO$_2$ and its doped/loaded counterparts is represented in Fig. 7B. The data processing applied (subtraction of the ATiO$_2$ absorption data) revealed an absorption band at around 380 nm for ATiO$_2$: Nb. This effect is probably due to the slight shift of the absorption edge which should result in a change in bandgap (Table 5).

After NH$_3$ treatment (ATiO$_2$: N), a new absorption band appeared clearly at around 440 nm (Fig. 7 A) which is amplified in Fig. 7B, as is the band at 380 nm due to a further shift of the absorption edge. This result can be considered as another evidence of N-doping even though N could hardly be detected by XPS.

Both phenomena are amplified for Nb, N-co-doped TiO$_2$ aerogel whose absorption is much stronger in the visible domain, as if a synergistic effect was at work.

The Cu-loaded samples (Cu/ATiO$_2$, Cu/ATiO$_2$:Nb, Cu/ATiO$_2$:N and Cu/ATiO$_2$: Nb, N) show some additional absorption in the range of 400 – 550 nm, which has already been observed by Li et al., [67] and attributed to the charge transfer from the valence band (VB) of TiO$_2$ to copper oxide nanoparticles. The absorption increased after Nb and N doping.

In the case of Cu/ATiO$_2$ and Cu/ATiO$_2$: Nb, which were not treated under NH$_3$, another absorption appeared in the range of 600 – 800 nm. This phenomenon can be associated with the intrinsic exciton band of CuO and the d–d transition of the Cu^{2+} species [68].

All these observations are consistent with the color of each sample (Fig. 7D). From ATiO$_2$ to ATiO$_2$: Nb, N, the samples' color shifts from white to beige due to a slight increase of absorption in the visible domain. The Cu-loaded samples absorb much more light. A minimum of absorption can be observed for Cu/ATiO$_2$ and Cu/ATiO$_2$: Nb in the green range of the visible spectrum (around 550 nm) which makes them

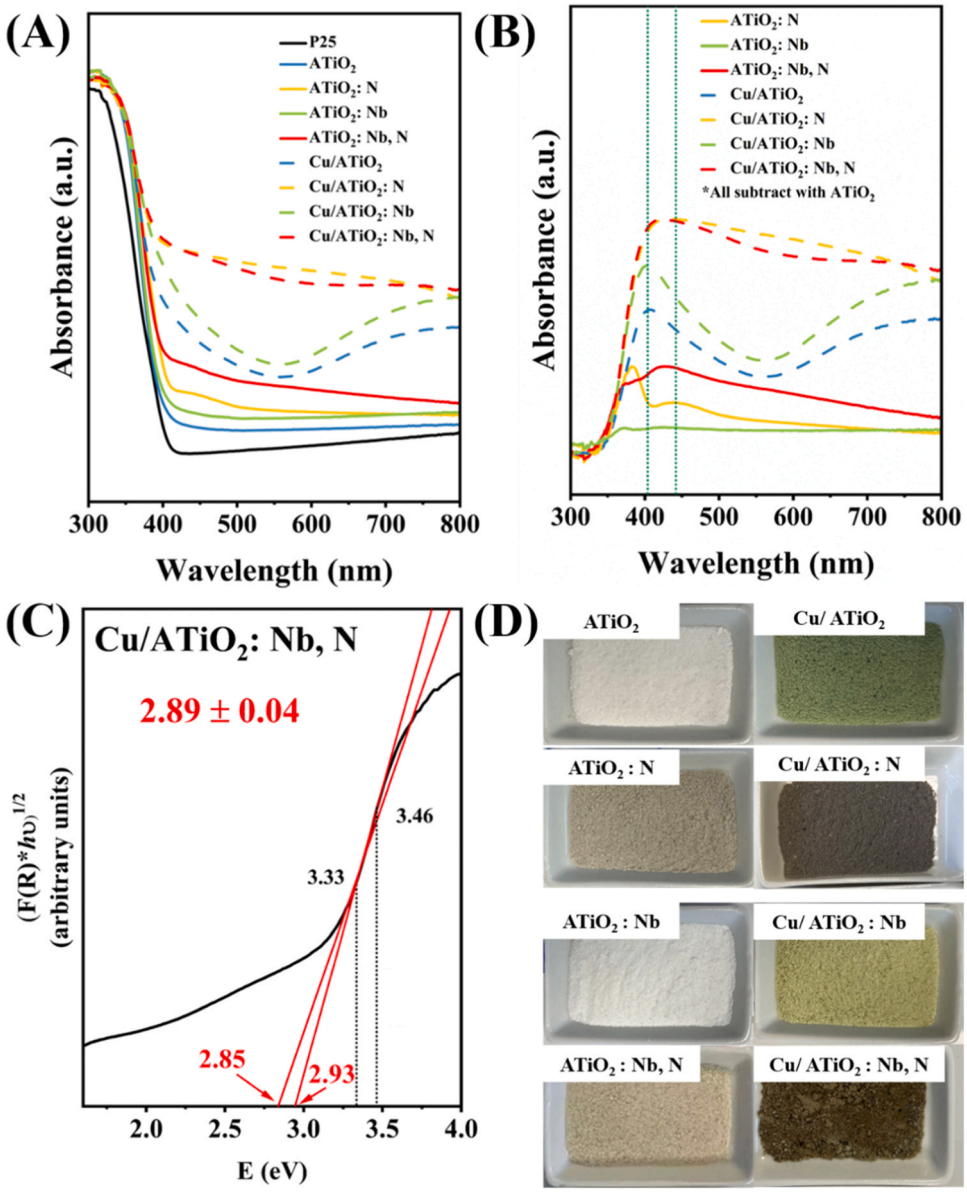

Fig. 7. (A) UV–vis diffuse reflectance spectra (UV-Vis DRS) of synthesized samples and P25, (B) spectra obtained after subtraction of that of $ATiO_2$, (C) Plot of the transformed Kubelka–Munk functions *vs.* the energy of light of Cu/$ATiO_2$: Nb, N and (D) samples images of $ATiO_2$, $ATiO_2$: N, $ATiO_2$: Nb, $ATiO_2$: Nb, N Cu/$ATiO_2$, Cu/$ATiO_2$: N, Cu/$ATiO_2$: Nb and Cu/$ATiO_2$: Nb, N.

Table 5
Band gap of P25 and as prepared samples.

Samples	Band gap (eV)
P25	3.03 ± 0.02
$ATiO_2$	3.04 ± 0.02
$ATiO_2$: N	3.00 ± 0.06
$ATiO_2$: Nb	3.00 ± 0.09
$ATiO_2$: Nb, N	2.97 ± 0.05
Cu/$ATiO_2$	2.96 ± 0.04
Cu/$ATiO_2$: N	2.92 ± 0.08
Cu/$ATiO_2$: Nb	2.93 ± 0.08
Cu/$ATiO_2$: Nb, N	2.89 ± 0.04

appear green. The samples treated in a reducing atmosphere (NH_3 treatment, Cu/$ATiO_2$: N and Cu/$ATiO_2$: Nb, N) do not show such a minimum and appear brown to dark grey.

The difference in light absorption observed for these different materials has an impact on their bandgap. This can be evidenced after Kubelka-Munk processing of the absorption data (Fig. 7 C and Table 5). Note that the bandgap values obtained for Cu-loaded samples have to be taken with caution since the presence of Cu oxides makes difficult the determination with Kubelka-Munk data treatment.

The absorbance spectrum of P25 shows a steep decrease between 350 and 400 nm, resulting in a bandgap of 3.03 eV in good agreement with previously reported data [69].

That of TiO_2 aerogel ($ATiO_2$) is very close (3.04 eV). It is clear from Fig. 7 A and 7D that the co-doping of $ATiO_2$, with Nb and N, enlarged the range of light absorption of TiO_2. As a consequence, its bandgap appeared to be slightly narrower than that of $ATiO_2$ and P25 with a value of 2.97 eV. Considering the accuracy of the calculation, it is difficult to sort these materials. However, with a value of 2.97 eV, the bandgap of $ATiO_2$: Nb, N is no doubt smaller than the expected one of 3.2 eV for classical anatase TiO_2. [70] The situation is even better after Cu deposition due to the charge transfer effect. The estimated bandgap of Cu/$ATiO_2$: Nb, N dropped to about 2.9 eV (provided that Cu oxides do not interfere with TiO_2), the smallest of all samples synthesized in this

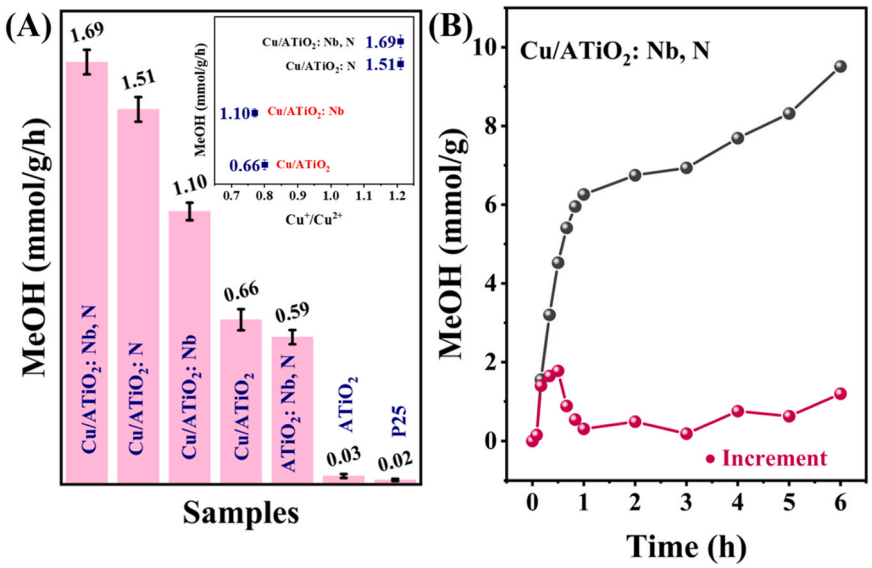

Fig. 8. (A) Photocatalytic evaluation via reduction of CO_2 under simulated Solar Light on synthesized materials compared to P25, the embedded figure representing the relationship between Methanol (MeOH) yield and Cu^+/Cu^{2+} ratio over Cu/ATiO$_2$: Nb, N, (B) MeOH yield per hour on Cu/ATiO$_2$: Nb, N.

study.

The bandgap of Cu/ATiO$_2$ doped with Nb or N, Cu/ATiO$_2$: Nb and Cu/ATiO$_2$: N, would stand in between that of Cu/ATiO$_2$ (2.96 eV) and that of Cu/ATiO$_2$: Nb, N (2.9 eV).

The doping with Nb is expected to decrease the bottom of the conduction band (CB) of TiO_2, while N doping should increase the top of the valence band (VB) of TiO_2 [17]. Thus, by doping with both Nb and N, the band gap of TiO_2 is expected to become narrower, improving the light absorption performance.

3.3. *Performance evaluation of photocatalytic CO_2 reduction*

Fig. 8A presents the performance of different photocatalysts to produce methanol (MeOH) through CO_2 photoreduction. Note that here we directly used a solution of Na_2CO_3 instead of directly bubbling CO_2 into H_2O as sometimes reported in the literature. The temperature does not exceed 35°C during the whole test (see Figure S2). In this work, the production rate was calculated throughout 6 h of illumination.

Undoped ATiO$_2$ showed a similar performance to the commercial catalyst P25 (0.03 ± 0.01 $mmol_{MeOH}/g_{cat}/h$ *vs* 0.02 ± 0.01 $mmol_{MeOH}/g_{cat}/h$), indicating that TiO_2 aerogel (ATiO$_2$) with higher specific surface area S_{BET} can compete with P25, a mix of anatase and rutile TiO_2. This confirms what we already observed in the case of water splitting and can thus be extended to CO_2 photoreduction.

The performance of co-doped ATiO$_2$, namely ATiO$_2$: Nb, N (0.59 ± 0.03 $mmol_{MeOH}/g_{cat}/h$) is much higher than that of ATiO$_2$ (0.03 ± 0.01 $mmol_{MeOH}/g_{cat}/h$). Doping with Nb and N improved MeOH production, probably due to the decrease of the bandgap resulting from changes in both the VB and CB energy levels in TiO_2.

The same level of performance can be reached with copper-loaded ATiO$_2$, Cu/ATiO$_2$ (0.66 ± 0.04 $mmol_{MeOH}/g_{cat}/h$). Here, the improvement may come from the ability of Cu_xO to improve the electron transfer efficiency during the reaction. Hence, we can conclude that both modifications have a similar impact on the performance even though their light absorption capacity is different. This also confirms that the mechanisms at work are much probably different.

Mixing both modifications has proven to be highly beneficial. Indeed, Cu/ATiO$_2$: Nb, N showed the best MeOH yield (1.69 ± 0.05 $mmol_{MeOH}/g_{cat}/h$), just before Cu/ATiO$_2$: N (1.51 ± 0.05 $mmol_{MeOH}/g_{cat}/h$) and Cu/ATiO$_2$: Nb (1.10 ± 0.04 $mmol_{MeOH}/g_{cat}/h$). Both N and Nb had a beneficial effect on the production of MeOH, but relatively, Cu/ATiO$_2$: N is more effective.

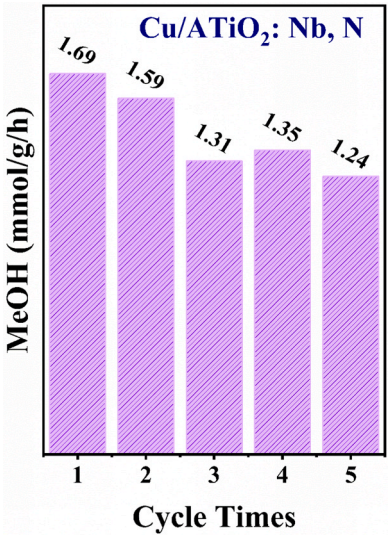

Fig. 9. Recycled use of Cu/ATiO$_2$: Nb, N for MeOH production from CO_2 photoreduction.

Looking back to Fig. 7 A, Cu/ATiO$_2$: N absorbs more light than Cu/ATiO$_2$: Nb. Moreover, XPS results showed that it has a higher Cu^+/Cu^{2+} ratio, similar to that of Cu/ATiO$_2$: Nb, N, which could also account for higher MeOH yields, due to the better ability of Cu^+ to favor the CO_2 hydrogenation process [71]. The same statement can be made for Cu/ATiO$_2$: Nb, N.

By comparing the production of MeOH on Cu/ATiO$_2$: Nb, N at different intervals of times during the reaction (Fig. 8B), the MeOH production rate was found to be the highest during the first hour after turning the light on (6 mmol/g/h). Then it gradually decreased to stabilize or so after 1 h (0.6 mmol/g/h). This will help to understand the reaction mechanism of CO_2 photocatalytic reduction.

We were also interested in the "recyclability" or reuse possibility of our catalyst. Fig. 9 shows the MeOH yields of Cu/ATiO$_2$: Nb, N tested 6 h, five times in a row. During the first runs, the MeOH yields slightly decreased from ~1.7 $mmol/g_{cat}/h$ to ~1.30 $mmol/g_{cat}/h$ in the third run before more or less stabilizing.

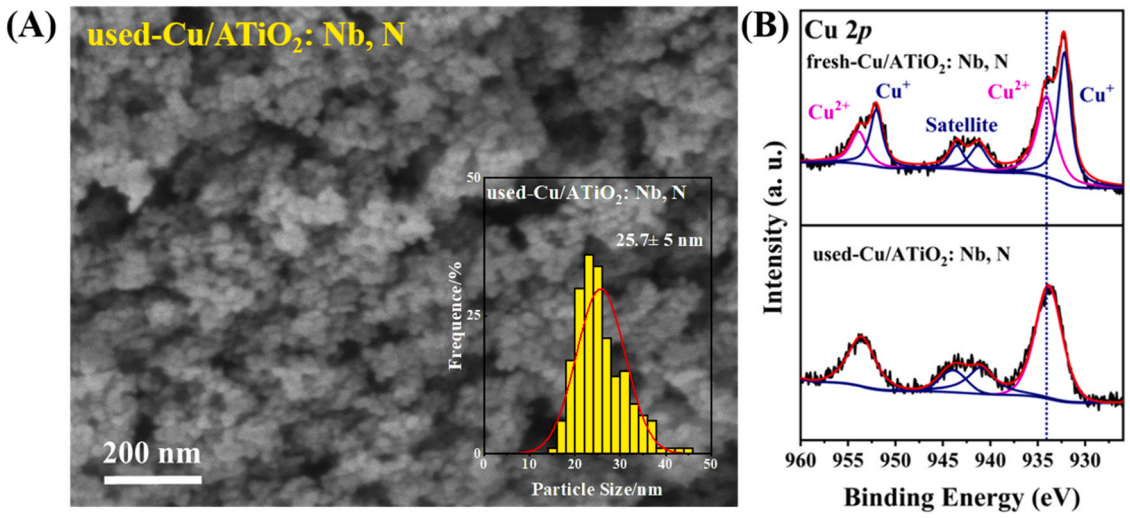

Fig. 10. (A) SEM image and Particle size distribution of used-Cu/ATiO$_2$: Nb, N and (B) Cu 2*p* XPS spectra of used-Cu/ATiO$_2$: Nb, N compare with fresh- Cu/ATiO$_2$: Nb, N.

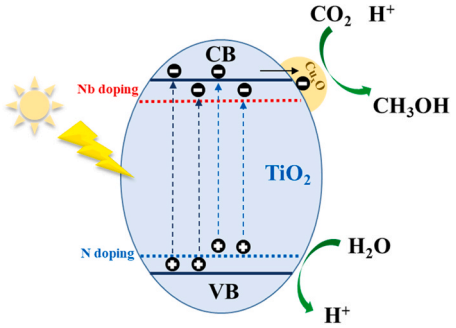

Scheme 2. Proposed reaction mechanism over Cu/ATiO$_2$: Nb, N.

To investigate the possible reasons for the slight decrease observed, the used catalyst was analyzed.

Firstly, the SEM image (Fig. 10 A) shows that the used-Cu/ATiO$_2$: Nb, N did not agglomerate after testing, instead, it remained as uniform and dispersed small sizes (~26 nm). So the morphology of the aerogel support remained stable after the test, which may not be the reason for loosing activity, and by the way, is good news for further long-term experiments.

Then the Cu 2*p* XPS spectrum of used-Cu/ATiO$_2$: Nb, N showed only Cu^{2+} species, whereas fresh-Cu/ATiO$_2$: Nb, N showed both Cu^{+} and Cu^{2+} species (Fig. 10B). This may partly explain the slight decrease in efficiency, caused by the conversion of $Cu^{+}\rightarrow Cu^{2+}$ on the catalyst surface during the reaction.

The mechanism of the photoreduction process is proposed, as shown in Scheme 2.

The photocatalytic process for converting CO_2 to methanol using Cu/ATiO$_2$: Nb, N involves a sequence of intricately linked steps, where both light absorption and charge separation are critical:

- Light Absorption: TiO_2 aerogel, when illuminated by the full-spectrum Xe lamp, absorbs photons across UV and visible wavelengths. This promotes electrons from the valence band to the conduction band, generating electron-hole pairs. The role of Nb and N doping here may extend beyond facilitating charge separation; it could also contribute to broadening the range of light absorption, particularly in the visible spectrum.
- Oxidation of Water: the process begins with the oxidation of water molecules or hydroxide ions on the TiO_2 surface, where the photogenerated holes in the valence band oxidize H_2O to O_2 and H^+ ions (protons). This step is crucial as it supplies the protons necessary for the subsequent reduction of CO_2.
- Role of Cu_xO Nanoparticles: acting as cocatalysts, Cu_xO nanoparticles capture the separated electrons and facilitate their transfer to CO_2, enhancing the reduction process and the overall yield of methanol.
- Reduction of CO_2: the photogenerated electrons in the conduction band, now more efficiently separated, are transferred to the surface where they meet with CO_2 and the protons. It is the reaction between CO_2, protons, and electrons that leads to the formation of methanol.
- Product Desorption: the methanol product, once formed, desorbs from the aerogel surface, which is then collected from the reaction mixture.

Table 6
Methanol production reported in the literature.

Photocatalyst	Testing conditions	Methanol yield	Testing time	References
Cu_xO/ATiO$_2$: Nb, N	CO_2 + Na_2CO_3 solution room temperature	10.14 mmol/g_{cat} (1.69 mmol/g_{cat}/h)	6 h	this work
NH2-MIL-125 (Ti)	CO_2 + 0.2 M EDA room temperature	7 mmol/g_{cat} (1.75 mmol/g_{cat}/h)	4 h	[72]
2% Pd-Cu/TiO_2	CO_2 + H_2O 50 °C	0.56 mmol/g_{cat} (0.07 mmol/g_{cat}/h)	8 h	[73]
Cu (II) ZIF	CO_2 + Na_2NO_3 solution room temperature	1.71 mmol/g_{cat} (0.342 mmol/g_{cat}/h)	5 h	[74]

Under dark conditions, as evidenced by our experiments listed in Table S3, no methanol production was detected, indicating that the reaction was light-driven. The high specific surface area of the TiO_2 aerogels contributes to the efficient adsorption of CO_2 and provides ample active sites for the reaction, while Nb and N doping, along with Cu_xO loading, collectively improve the TiO_2's optical properties and charge carrier dynamics, crucial for the effective photoreduction of CO_2 to methanol.

Finally, we compared our work to reported ones in the literature and

realized in similar testing conditions, as far as the comparison is possible (See Table 6).

Our photocatalyst could reach the best performance ever published, in a longer period of time.

4. Conclusions

In conclusion, Cu_xO-loaded, Nb, and N co-doped TiO_2 aerogels (Cu/$ATiO_2$: Nb, N) were synthesized by the sol-gel method, supercritical CO_2 drying, and gas phase doping. $ATiO_2$ showed an anatase phase with particle size around 20–30 nm. Cu_xO was uniformly distributed on the TiO_2 surface with particle size < 2 nm. Nb and N doping enhanced the light absorption properties of TiO_2 and narrowed its bandgap. Loading with Cu_xO improved the electron transfer efficiency and the visible light absorption ability.

Applied for CO_2 photocatalytic reduction, Cu/$ATiO_2$: Nb, N has shown to have the best performance and the highest MeOH yield (1.69 ± 0.05 mmol/g_{cat}/h). This can be ascribed to several factors: i) improved optical properties after doping; ii) uniform distribution of Cu species in the surface and bulk of TiO_2; iii) high specific surface area and particle connectivity resulting from the peculiar aerogel morphology. These factors all contribute to enhancing the performance of TiO_2 for CO_2 reduction and MeOH production.

The finding that Cu/TiO_2 with Nb and N co-doping has the best performance in CO_2 reduction and the highest MeOH yield is very promising. This material could be a highly effective photocatalyst for the CO_2 reduction process. Further research and development on the aerogel morphology or N-doping will lead to the optimization of this material for such an application. The stability was revealed to be quite good but can however be improved, for example through stabilization of Cu^+ on the catalyst surface.

CRediT authorship contribution statement

Mourad Benabdesselam: Data curation. **Christian Beauger:** Writing – review & editing, Validation, Supervision, Conceptualization. **Miaomiao Wen:** Writing – review & editing, Writing – original draft, Investigation, Formal analysis, Data curation.

Declaration of Competing Interest

The authors declare that they have no known competing financial interests or personal relationships that could have appeared to influence the work reported in this paper.

Data availability

Data will be made available on request.

Acknowledgments

This work was supported by the China Scholarship Council (202006880014) and ARMINES.

The authors thank Frédéric Georgi and Gabriel Monge from MINES Paris – CEMEF, Ileana Florea from CNRS-CRHEA and Julien Jaxel and Cédric Sernissi from MINES Paris – PERSEE for their contribution to XPS, XRD, TEM, SEM, and photocatalytic tests.

Appendix A. Supporting information

Supplementary data associated with this article can be found in the online version at doi:10.1016/j.jcou.2024.102719.

References

[1] C. Mardones, N. Baeza, Economic and environmental effects of a CO2 tax in Latin American Countries, Energy Policy *114* (2018) 262–273, https://doi.org/10.1016/j.enpol.2017.12.001.
[2] L.A. Curtiss, K. Raghavachari, P.C. Redfern, J.A. Pople, Assessment of Gaussian-2 and density functional theories for the computation of enthalpies of formation, J. Chem. Phys. *106* (3) (1997) 1063–1079, https://doi.org/10.1063/1.473182.
[3] X. Chang, T. Wang, J. Gong, CO2 Photo-reduction: insights into CO2 activation and reaction on surfaces of photocatalysts, Energy Environ. Sci. *9* (7) (2016) 2177–2196, https://doi.org/10.1039/C6EE00383D.
[4] P.D. Tran, L.H. Wong, J. Barber, J.S.C. Loo, Recent advances in hybrid photocatalysts for solar fuel production, Energy Environ. Sci. *5* (3) (2012) 5902–5918, https://doi.org/10.1039/C2EE02849B.
[5] J. Schneider, H. Jia, J.T. Muckerman, E. Fujita, Thermodynamics and kinetics of CO2, CO, and H+ binding to the metal centre of CO2 reduction catalysts, Chem. Soc. Rev. *41* (6) (2012) 2036–2051, https://doi.org/10.1039/C1CS15278E.
[6] K. Nakata, A. Fujishima, TiO2 Photocatalysis: Design and Applications, J. Photochem. Photobiol. C. Photochem. Rev. *13* (3) (2012) 169–189, https://doi.org/10.1016/j.jphotochemrev.2012.06.001.
[7] T. Inoue, A. Fujishima, S. Konishi, K. Honda, Photoelectrocatalytic Reduction of Carbon Dioxide in Aqueous Suspensions of Semiconductor Powders, Nature *277* (5698) (1979) 637–638, https://doi.org/10.1038/277637a0.
[8] A. Khalilzadeh, A. Shariati, Photoreduction of CO2 over Heterogeneous Modified TiO2 Nanoparticles under Visible Light Irradiation: Synthesis, Process and Kinetic Study, Sol. Energy *164* (2018) 251–261, https://doi.org/10.1016/j.solener.2018.02.063.
[9] L. Zhang, M. Jaroniec, Toward Designing Semiconductor-Semiconductor Heterojunctions for Photocatalytic Applications, Appl. Surf. Sci. *430* (2018) 2–17, https://doi.org/10.1016/j.apsusc.2017.07.192.
[10] P.S. Basavarajappa, S.B. Patil, N. Ganganagappa, K.R. Reddy, A.V. Raghu, Ch. V. Reddy, Recent Progress in Metal-Doped TiO2, Non-Metal Doped/Codoped TiO2 and TiO2 Nanostructured Hybrids for Enhanced Photocatalysis, Int. J. Hydrog. Energy *45* (13) (2020) 7764–7778, https://doi.org/10.1016/j.ijhydene.2019.07.241.
[11] S. Lettieri, M. Pavone, A. Fioravanti, L. Santamaria Amato, P. Maddalena, Charge Carrier Processes and Optical Properties in TiO2 and TiO2-Based Heterojunction Photocatalysts: A Review, Materials *14* (7) (2021) 1645, https://doi.org/10.3390/ma14071645.
[12] S. Al Jitan, G. Palmisano, C. Garlisi, Synthesis and Surface Modification of TiO2-Based Photocatalysts for the Conversion of CO2, Catalysts *10* (2) (2020) 227, https://doi.org/10.3390/catal10020227.
[13] L.-W. Zhang, H.-B. Fu, Y.-F. Zhu, Efficient TiO2 Photocatalysts from Surface Hybridization of TiO2 Particles with Graphite-like Carbon, Adv. Funct. Mater. *18* (15) (2008) 2180–2189, https://doi.org/10.1002/adfm.200701478.
[14] A. Khlyustova, N. Sirotkin, T. Kusova, A. Kraev, V. Titov, A. Agafonov, Doped TiO2: The Effect of Doping Elements on Photocatalytic Activity, Mater. Adv. *1* (5) (2020) 1193–1201, https://doi.org/10.1039/D0MA00171F.
[15] J.F. Houlihan, D.B. Armitage, T. Hoovler, D. Bonaquist, D.P. Madacsi, L.N. Mulay, Doped Polycrystalline TiO2 Electrodes for the Photo-Assisted Electrolysis of Water, Mater. Res. Bull. *13* (11) (1978) 1205–1212, https://doi.org/10.1016/0025-5408(78)90210-6.
[16] W. Choi, A. Termin, M.R. Hoffmann, The Role of Metal Ion Dopants in Quantum-Sized TiO2: Correlation between Photoreactivity and Charge Carrier Recombination Dynamics, J. Phys. Chem. *98* (51) (1994) 13669–13679, https://doi.org/10.1021/j100102a038.
[17] R. Asahi, T. Morikawa, T. Ohwaki, K. Aoki, Y. Taga, Visible-Light Photocatalysis in Nitrogen-Doped Titanium Oxides, Science *293* (5528) (2001) 269–271, https://doi.org/10.1126/science.1061051.
[18] M. Fujihira, Y. Satoh, T. Osa, Heterogeneous Photocatalytic Oxidation of Aromatic Compounds on TiO2, Nature *293* (5829) (1981) 206–208, https://doi.org/10.1038/293206a0.
[19] D. Gogoi, A. Namdeo, A.K. Golder, N.R. Peela, Ag-Doped TiO2 Photocatalysts with Effective Charge Transfer for Highly Efficient Hydrogen Production through Water Splitting, Int. J. Hydrog. Energy *45* (4) (2020) 2729–2744, https://doi.org/10.1016/j.ijhydene.2019.11.127.
[20] K.P. Priyanka, V.R. Revathy, P. Rosmin, B. Thrivedu, K.M. Elsa, J. Nimmymol, K. M. Balakrishna, T. Varghese, Influence of La Doping on Structural and Optical Properties of TiO2 Nanocrystals, Mater. Charact. *113* (2016) 144–151, https://doi.org/10.1016/j.matchar.2016.01.015.
[21] C. Tian, W. Sheng, H. Tan, H. Jiang, C. Xiong, Fabrication of Lattice-Doped TiO2 Nanofibers by Vapor-Phase Growth for Visible Light-Driven N2 Conversion to Ammonia, ACS Appl. Mater. Interfaces *10* (43) (2018) 37453–37460, https://doi.org/10.1021/acsami.8b15174.
[22] S.X. Zhang, D.C. Kundaliya, W. Yu, S. Dhar, S.Y. Young, L.G. Salamanca-Riba, S. B. Ogale, R.D. Vispute, T. Venkatesan, Niobium Doped TiO2: Intrinsic Transparent Metallic Anatase versus Highly Resistive Rutile Phase, J. Appl. Phys. *102* (1) (2007) 013701, https://doi.org/10.1063/1.2750407.
[23] T. Hitosugi, H. Kamisaka, K. Yamashita, H. Nogawa, Y. Furubayashi, S. Nakao, N. Yamada, A. Chikamatsu, H. Kumigashira, M. Oshima, Y. Hirose, T. Shimada, T. Hasegawa, Electronic Band Structure of Transparent Conductor: Nb-Doped Anatase TiO2, Appl. Phys. Express *1* (11) (2008) 111203, https://doi.org/10.1143/APEX.1.111203.
[24] W. Xu, P.A. Russo, T. Schultz, N. Koch, N. Pinna, Niobium-Doped Titanium Dioxide with High Dopant Contents for Enhanced Lithium-Ion Storage, ChemElectroChem *7* (19) (2020) 4016–4023, https://doi.org/10.1002/celc.202001040.

[25] J. Yue, C. Suchomski, P. Voepel, R. Ellinghaus, M. Rohnke, T. Leichtweiss, M. T. Elm, B.M. Smarsly, Mesoporous Niobium-Doped Titanium Dioxide Films from the Assembly of Crystalline Nanoparticles: Study on the Relationship between the Band Structure, Conductivity and Charge Storage Mechanism, J. Mater. Chem. A *5* (5) (2017) 1978–1988, https://doi.org/10.1039/C6TA06840E.

[26] H.-Y. Lee, J. Robertson, Doping and Compensation in Nb-Doped Anatase and Rutile TiO2, J. Appl. Phys. *113* (21) (2013) 213706, https://doi.org/10.1063/1.4808475.

[27] *Oxygen Rich Titania: A Dopant Free, High Temperature Stable, and Visible-Light Active Anatase Photocatalyst - Etacheri - 2011 - Advanced Functional Materials - Wiley Online Library*. https://onlinelibrary.wiley.com/doi/full/10.1002/adfm.201100301 (accessed 2023–07-21).

[28] L. Kong, C. Wang, H. Zheng, X. Zhang, Y. Liu, Defect-Induced Yellow Color in Nb-Doped TiO2 and Its Impact on Visible-Light Photocatalysis, J. Phys. Chem. C. *119* (29) (2015) 16623–16632, https://doi.org/10.1021/acs.jpcc.5b03448.

[29] F. Dong, S. Guo, H. Wang, X. Li, Z. Wu, Enhancement of the Visible Light Photocatalytic Activity of C-Doped TiO2 Nanomaterials Prepared by a Green Synthetic Approach, J. Phys. Chem. C. *115* (27) (2011) 13285–13292, https://doi.org/10.1021/jp111916q.

[30] J.T. Park, D.J. Kim, D.H. Kim, J.H. Kim, A Facile Graft Polymerization Approach to N-Doped TiO2 Heterostructures with Enhanced Visible-Light Photocatalytic Activity, Mater. Lett. *202* (2017) 66–69, https://doi.org/10.1016/j.matlet.2017.05.070.

[31] L. Bergamonti, G. Predieri, Y. Paz, L. Fornasini, P.P. Lottici, F. Bondioli, Enhanced Self-Cleaning Properties of N-Doped TiO2 Coating for Cultural Heritage, Microchem. J. *133* (2017) 1–12, https://doi.org/10.1016/j.microc.2017.03.003.

[32] F. Veisi, M.A. Zazouli, M.A. Ebrahimzadeh, J.Y. Charati, A.S. Dezfoli, Photocatalytic Degradation of Furfural in Aqueous Solution by N-Doped Titanium Dioxide Nanoparticles, Environ. Sci. Pollut. Res. *23* (21) (2016) 21846–21860, https://doi.org/10.1007/s11356-016-7199-7.

[33] Y.J. Hwang, S. Yang, H. Lee, Surface Analysis of N-Doped TiO2 Nanorods and Their Enhanced Photocatalytic Oxidation Activity, Appl. Catal. B Environ. *204* (2017) 209–215, https://doi.org/10.1016/j.apcatb.2016.11.038.

[34] W. Zhang, Q. Zhou, N. Li, M. Li, Enhanced Photocatalytic Reduction of CO2 into CH4 over N, Eu Co-Doped TiO2: Insight into the Synergistic Effect of N and Eu, Appl. Catal. Gen. (2022) 118977, https://doi.org/10.1016/j.apcata.2022.118977.

[35] M. Nasir, S. Bagwasi, Y. Jiao, F. Chen, B. Tian, J. Zhang, Characterization and Activity of the Ce and N Co-Doped TiO2 Prepared through Hydrothermal Method, Chem. Eng. J. *236* (2014) 388–397, https://doi.org/10.1016/j.cej.2013.09.095.

[36] W.-C. Hung, Y.-C. Chen, H. Chu, T.-K. Tseng, Synthesis and Characterization of TiO2 and Fe/TiO2 Nanoparticles and Their Performance for Photocatalytic Degradation of 1,2-Dichloroethane, Appl. Surf. Sci. *255* (5, Part 1) (2008) 2205–2213, https://doi.org/10.1016/j.apsusc.2008.07.079.

[37] I.-H. Tseng, J.C.S. Wu, H.-Y. Chou, Effects of Sol–Gel Procedures on the Photocatalysis of Cu/TiO2 in CO2 Photoreduction, J. Catal. *221* (2) (2004) 432–440, https://doi.org/10.1016/j.jcat.2003.09.002.

[38] C. Zhao, A. Krall, H. Zhao, Q. Zhang, Y. Li, Ultrasonic Spray Pyrolysis Synthesis of Ag/TiO2 Nanocomposite Photocatalysts for Simultaneous H2 Production and CO2 Reduction, Int. J. Hydrog. Energy *37* (13) (2012) 9967–9976, https://doi.org/10.1016/j.ijhydene.2012.04.003.

[39] Au@TiO2 Core–Shell Composites for the Photocatalytic Reduction of CO2 - Pougin - 2018 - *Chemistry – A European Journal - Wiley Online Library*. ⟨https://chemistry-europe.onlinelibrary.wiley.com/doi/10.1002/chem.201801796⟩ (accessed 2023-05-09).

[40] M. Tasbihi, K. Kočí, M. Edelmannová, I. Troppová, M. Reli, R. Schomäcker, Pt/TiO2 Photocatalysts Deposited on Commercial Support for Photocatalytic Reduction of CO2, J. Photochem. Photobiol. Chem. *366* (2018) 72–80, https://doi.org/10.1016/j.jphotochem.2018.04.012.

[41] S. Bie, Q. Liu, M. Wen, X. Ye, C. Xiong, Preparation of P-Aminobenzoic Acid Grafted TiO x Semiconductive Aerogels for Photocatalytic Reduction of CO 2 to Methanol, N. J. Chem. *45* (16) (2021) 7154–7162.

[42] X. Chen, X. Ye, J. He, L. Pan, S. Xu, C. Xiong, Preparation of Fe3+-Doped TiO2 Aerogels for Photocatalytic Reduction of CO2 to Methanol, J. Sol. -Gel Sci. Technol. *95* (2) (2020) 353–359, https://doi.org/10.1007/s10971-020-05260-9.

[43] X. Yang, D. Wang, Photocatalysis: From Fundamental Principles to Materials and Applications, ACS Appl. Energy Mater. *1* (12) (2018) 6657–6693, https://doi.org/10.1021/acsaem.8b01345.

[44] M. Wen, B. Ren, X. Ye, J. He, H. Jiang, C. Xiong, Hierarchical Loading of CuO on SiO2 Aerogel@high Crystalline TiO2 Nanofibers for Efficiently Photocatalytic Reduction of CO2 without Sacrificial Agent, Nano Res *15* (5) (2022) 3872–3879, https://doi.org/10.1007/s12274-021-3994-7.

[45] G. Dagan, M. Tomkiewicz, Preparation and Characterization of TiO2 Aerogels for Use as Photocatalysts, J. Non-Cryst. Solids *175* (2) (1994) 294–302, https://doi.org/10.1016/0022-3093(94)90023-X.

[46] L. Zhang, L. Dai, X. Li, W. Yu, S. Li, J. Guan, 3D Structured TiO2-Based Aerogel Photocatalyst for the High-Efficiency Degradation of Toluene Gas, N. J. Chem. *46* (5) (2022) 2272–2281, https://doi.org/10.1039/D1NJ05395G.

[47] A.L. Luna, F. Matter, M. Schreck, J. Wohlwend, E. Tervoort, C. Colbeau-Justin, M. Niederberger, Monolithic Metal-Containing TiO2 Aerogels Assembled from Crystalline Pre-Formed Nanoparticles as Efficient Photocatalysts for H2 Generation, Appl. Catal. B Environ. *267* (2020) 118660, https://doi.org/10.1016/j.apcatb.2020.118660.

[48] J. Wan, L.-H. Xu, H. Pan, L.-M. Wang, Y. Shen, Green Water-Based Fabrication of SiO2–TiO2 Aerogels with Superhydrophobic and Photocatalytic Properties and Their Application on Cotton Fabric, J. Porous Mater. *28* (5) (2021) 1501–1510, https://doi.org/10.1007/s10934-021-01089-x.

[49] H. Xiong, Y. Dong, D. Liu, R. Long, T. Kong, Y. Xiong, Recent Advances in Porous Materials for Photocatalytic CO2 Reduction, J. Phys. Chem. Lett. *13* (5) (2022) 1272–1282, https://doi.org/10.1021/acs.jpclett.1c03204.

[50] C. Beauger, L. Testut, S. Berthon-Fabry, F. Georgi, L. Guetaz, Doped TiO2 Aerogels as Alternative Catalyst Supports for Proton Exchange Membrane Fuel Cells: A Comparative Study of Nb, V and Ta Dopants, Microporous Mesoporous Mater. *232* (2016) 109–118, https://doi.org/10.1016/j.micromeso.2016.06.003.

[51] S. Boujday, F. Wünsch, P. Portes, J.-F. Bocquet, C. Colbeau-Justin, Photocatalytic and Electronic Properties of TiO2 Powders Elaborated by Sol–Gel Route and Supercritical Drying, Sol. Energy Mater. Sol. Cells *83* (4) (2004) 421–433, https://doi.org/10.1016/j.solmat.2004.02.035.

[52] D. D'Elia, C. Beauger, J.-F. Hochepied, A. Rigacci, M.-H. Berger, N. Keller, V. Keller-Spitzer, Y. Suzuki, J.-C. Valmalette, M. Benabdesselam, P. Achard, Impact of Three Different TiO2 Morphologies on Hydrogen Evolution by Methanol Assisted Water Splitting: Nanoparticles, Nanotubes and Aerogels, Int. J. Hydrog. Energy *36* (22) (2011) 14360–14373, https://doi.org/10.1016/j.ijhydene.2011.08.007.

[53] B. Erdem, R.A. Hunsicker, G.W. Simmons, E.D. Sudol, V.L. Dimonie, M.S. El-Aasser, XPS and FTIR Surface Characterization of TiO2 Particles Used in Polymer Encapsulation, Langmuir *17* (9) (2001) 2664–2669, https://doi.org/10.1021/la0015213.

[54] G. Ou, Y. Xu, B. Wen, R. Lin, B. Ge, Y. Tang, Y. Liang, C. Yang, K. Huang, D. Zu, R. Yu, W. Chen, J. Li, H. Wu, L.-M. Liu, Y. Li, Tuning Defects in Oxides at Room Temperature by Lithium Reduction, Nat. Commun. *9* (1) (2018) 1302, https://doi.org/10.1038/s41467-018-03765-0.

[55] M.Z. Atashbar, H.T. Sun, B. Gong, W. Wlodarski, R. Lamb, XPS Study of Nb-Doped Oxygen Sensing TiO2 Thin Films Prepared by Sol-Gel Method, Thin Solid Films *326* (1–2) (1998) 238–244, https://doi.org/10.1016/S0040-6090(98)00534-3.

[56] C. Foo, Y. Li, K. Lebedev, T. Chen, S. Day, C. Tang, S.C.E. Tsang, Characterisation of Oxygen Defects and Nitrogen Impurities in TiO2 Photocatalysts Using Variable-Temperature X-Ray Powder Diffraction, Nat. Commun. *12* (1) (2021) 661, https://doi.org/10.1038/s41467-021-20977-z.

[57] P. Basnet, E. Anderson, Y. Zhao, Hybrid CuxO–TiO2 Nanopowders Prepared by Ball Milling for Solar Energy Conversion and Visible-Light-Induced Wastewater Treatment, ACS Appl. Nano Mater. *2* (4) (2019) 2446–2455, https://doi.org/10.1021/acsanm.9b00325.

[58] J. Li, Z. Mei, L. Liu, H. Liang, A. Azarov, A. Kuznetsov, Y. Liu, A. Ji, Q. Meng, X. Du, Probing Defects in Nitrogen-Doped Cu2O, Sci. Rep. *4* (1) (2014) 7240, https://doi.org/10.1038/srep07240.

[59] W. Gordy, W.J.O. Thomas, Electronegativities of the Elements, J. Chem. Phys. *24* (2) (2004) 439–444, https://doi.org/10.1063/1.1742493.

[60] M. Abdennouri, A. Elhalil, M. Farnane, H. Tounsadi, F.Z. Mahjoubi, R. Elmoubarki, M. Sadiq, L. Khamar, A. Galadi, M. Baâlala, Photocatalytic Degradation of 2, 4-D and 2, 4-DP Herbicides on Pt/TiO2 Nanoparticles, J. Saudi Chem. Soc. *19* (5) (2015) 485–493.

[61] D.R. Eddy, G.A. Nur Sheha, M.D. Permana, N. Saito, T. Takei, N. Kumada, Irkham, I. Rahayu, I. Abe, Y. Sekine, T. Oyumi, Y. Izumi, Study on Triphase of Polymorphs TiO2 (Anatase/Rutile/Brookite) for Boosting Photocatalytic Activity of Metformin Degradation, Chemosphere (2024) 141206, https://doi.org/10.1016/j.chemosphere.2024.141206.

[62] G. Dagan, M. Tomkiewicz, Titanium Dioxide Aerogels for Photocatalytic Decontamination of Aquatic Environments, J. Phys. Chem. *97* (49) (1993) 12651–12655, https://doi.org/10.1021/j100151a001.

[63] M.K. Mehrizi, S.M. Mortazavi, S. Mallakpour, S.M. Bidoki, The Effect of Nano- and Micro-TiO2 Particles on Reflective Behavior of Printed Cotton/Nylon Fabrics in Vis/NIR Regions, Color Res. Appl. *37* (3) (2012) 199–205, https://doi.org/10.1002/col.20675.

[64] S. Chen, A.M. Abdel-Mageed, D. Li, J. Bansmann, S. Cisneros, J. Biskupek, W. Huang, R.J. Behm, Morphology-Engineered Highly Active and Stable Ru/TiO2 Catalysts for Selective CO Methanation, Angew. Chem. Int. Ed. *58* (31) (2019) 10732–10736, https://doi.org/10.1002/anie.201903882.

[65] D.A. Svintsitskiy, T.Yu Kardash, O.A. Stonkus, E.M. Slavinskaya, A.I. Stadnichenko, S.V. Koscheev, A.P. Chupakhin, A.I. Boronin, In Situ XRD, XPS, TEM, and TPR Study of Highly Active in CO Oxidation CuO Nanopowders, J. Phys. Chem. C. *117* (28) (2013) 14588–14599, https://doi.org/10.1021/jp403339r.

[66] Q. Shi, Y. Li, E. Zhan, N. Ta, W. Shen, Anatase TiO2 Hollow Nanosheets: Dual Roles of F−, Formation Mechanism, and Thermal Stability, CrystEngComm *16* (16) (2014) 3431–3437, https://doi.org/10.1039/C3CE42580K.

[67] B. Li, Y. Hao, B. Zhang, X. Shao, L. Hu, A Multifunctional Noble-Metal-Free Catalyst of CuO/TiO2 Hybrid Nanofibers, Appl. Catal. Gen. *531* (2017) 1–12, https://doi.org/10.1016/j.apcata.2016.12.002.

[68] Y. Zeng, T. Wang, S. Zhang, Y. Wang, Q. Zhong, Sol–Gel Synthesis of CuO-TiO2 Catalyst with High Dispersion CuO Species for Selective Catalytic Oxidation of NO, Appl. Surf. Sci. *411* (2017) 227–234, https://doi.org/10.1016/j.apsusc.2017.03.107.

[69] L. Yu, Y. Lin, J. Huang, S. Lin, D. Li, A Visible Light Photocatalyst of Carbonate-Like Species Doped TiO2, J. Am. Ceram. Soc. *100* (1) (2017) 333–342, https://doi.org/10.1111/jace.14552.

[70] Y. Mi, Y. Weng, Band Alignment and Controllable Electron Migration between Rutile and Anatase TiO2, Sci. Rep. *5* (1) (2015) 11482, https://doi.org/10.1038/srep11482.

[71] J. Zhang, X. Sun, C. Wu, W. Hang, X. Hu, D. Qiao, B. Yan, Engineering Cu+/CeZrOx Interfaces to Promote CO2 Hydrogenation to Methanol, J. Energy Chem. *77* (2023) 45–53, https://doi.org/10.1016/j.jechem.2022.10.034.

[72] Y. Zhao, X. Ye, Y. Liu, Y. Deng, M. Wen, J. He, H. Jiang, C. Xiong, Fabrication of Glass Immobilized Amorphous Organotitanium Polymer for Enhancing Catalytic

Turnover Frequency and Stabilities in Photocatalytic Reduction of CO2, Appl. Catal. Gen. *647* (2022) 118910, https://doi.org/10.1016/j.apcata.2022.118910.

[73] X. Shang, G. Li, R. Wang, T. Xie, J. Ding, Q. Zhong, Precision Loading of Pd on Cu Species for Highly Selective CO2 Photoreduction to Methanol, Chem. Eng. J. *456* (2023) 140805, https://doi.org/10.1016/j.cej.2022.140805.

[74] J. Li, D. Luo, C. Yang, S. He, S. Chen, J. Lin, L. Zhu, X. Li, Copper(II) Imidazolate Frameworks as Highly Efficient Photocatalysts for Reduction of CO2 into Methanol under Visible Light Irradiation, J. Solid State Chem. *203* (2013) 154–159, https://doi.org/10.1016/j.jssc.2013.04.016.